Molecularly Engineered Thienyl-Triphenylamine Substituted Zinc Phthalocyanine as Dopant Free Hole Transporting Materials in Perovskite Solar Cells

Peng Huang,[a] Adrián Hernández,[b] Samrana Kazim,[a,c] Javier Ortíz,[b] Ángela Sastre-Santos,[*b] and Shahzada Ahmad [*a,c]

[a]BCMaterials, Basque Center for Materials, Applications and Nanostructures, UPV/EHU Science Park, 48940 Leioa, Spain, Tel: +34 946128811

E-mail: shahzada.ahmad@bcmaterials.net

[b]Área de Química Orgánica, Instituto de Bioingeniería Universidad Miguel Hernández Avda. de la Universidad, s/n, Elche 03202, Spain E-mail: asastre@umh.es

[c]IKERBASQUE, Basque Foundation for Science, Bilbao, 48013, Spain

Abstract

To endure the success of perovskite solar cells (PSCs), developing dopant-free hole transporting materials is of paramount importance to induce long-term stability. Phthalocyanine has emerged as a viable alternative for common Spiro-OMeTAD, due to their excellent optoelectrical properties and chemical stability. We report the design and semiconducting properties of a thienyl-triphenylamine tetrasubstituted Zinc (II) phthalocyanine, and its application into PSCs. The PSCs fabricated with Zinc phthalocyanine without the use of any dopant and additives gave a competitive power conversion efficiency in excess of 14.5%, along with long-term stability.

Introduction

The last decade has witnessed an enormous development in the investigation of organic-inorganic hybrid perovskite solar cells (PSCs) due to their power conversion efficiency (PCE) skyrocketing from 3.8% to 25.2%.[1–5] This rapid development is owing to the outstanding properties of organic-inorganic halide perovskites: panchromatic light absorption and long-range ambipolar carrier diffusion as well as the choice of solution-processability at low temperature.[6–8] In the device configuration of PSCs, the light harvester perovskites layers are sandwiched between an electron and hole transporting material (ETM, HTM). This can be categorized into normal (*n-i-p*) and inverted (*p-i-n*) structures according to whether ETM or HTM is in contact with the bottom transparent conductive electrode (TCO).

In a standard normal device structure (TCO/ETM/perovskite/HTM/metal electrode), HTMs atop of perovskite layer play pivotal roles in achieving high efficiency and long-term stability in PSCs. The hole transporting layers extract and transport photo-generated holes from perovskite to the metal electrode rapidly, avoiding undesired charge recombination losses at the interfaces and also inhibits the degradation process induced by oxygen and moisture.[9–11] An effective HTM must fulfill the following requirements: simplified synthesis procedure, solution-processability, uniform film formation (compact morphology) without any pinhole, the relatively high charge transporting abilities, the well aligned highest occupied molecular orbital (HOMO) /valence band with valence band of perovskite, superior stability under ambient and thermal condition.[12–15]

To date, *2,2´,7,7´*-tetrakis-(*N,N*-di-p, methoxyphenylamine)-9,9´-spirobifluorene (Spiro-OMeTAD) is most investigated HTM in *n-i-p* structure type devices because of their simple orthogonal solution-processability (to common perovskites) and high performance of the devices.[16–21] However, Spiro-OMeTAD possesses low conductivity and mobility in its pristine form, and introducing a hygroscopic *p*-type dopant and additive such as lithium bis(trifluoromethanesulfonyl)imide (Li-TFSI) and 4-tert-Butylpyridine (t-BP) is prerequisite to enhance the charge transporting ability of Spiro-OMeTAD, but on the contrary, this can also accelerate the degradation of perovskite and lowers the stability of the fabricated devices. The tedious multi-step synthesis and costly purification process of Spiro-OMeTAD along with the use of indispensable hydrophilic dopants and additives limits its further extensive application in PSCs.[22,23]

Recently, among alternatives that meet HTM's criteria, including small molecules, conjugated polymers, and inorganic p-type semiconductors , *etc.*, have been specially designed and synthesized to supersede Spiro-OMeTAD.[12,14,15,24–26] Among them, one such promising category of attractive HTM is metal phthalocyanine (Pcs), analogs which own organic macrocycles with an extended π-conjugated system and planar structure.[27–30] They are cost-effective and attractive due to their facile synthesis and purification, high hydrophobicity, as well as excellent stability under thermal and photo conditions. Moreover, they exhibit a unique combination of chemical, optical and electronic properties that can be tailored by molecular engineering. The peripheral and non-peripheral substitution of Pcs is an effective approach to regulate their chemical and electrical properties. [29,31,32] The efficiency of

Pcs-based PSC was significantly improved to nearly 20% since the first paper reported on vacuum-deposited CuPc in PSCs in 2015.[33–35] Catchpole *et al.* applied solution-processed copper (II) 2,9,16,23-tetra-tert-butyl-29*H*,31*H*-phthalocyanine as a doped HTM for PSCs and reported the highest efficiency of the device with Pcs.[35] Recently, Pc derivatives have emerged as an appealing dopant-free HTMs.[27,36–39] Dopant-free Zinc (II) 2,9,16,23-tetra-tert-butyl-29*H*,31*H*-phthalocyanine dimers with 3,6-bisthienylldiketopyrrolopyrrole (ZnPc-DPP-ZnPc) as dopant-free HTM into PSCs yielded 16.8% PCE.[40] Similarly, Wang *et al.* successfully developed tetra-methoxyl triphenylamine substituted zinc phthalocyanine (OTPA-ZnPc) as a dopant-free HTM, and corresponding device gave 16.23% efficiency.[41] Xu *et al.* investigated properties and application of two CuPcs: methoxydiphenylamine / methoxy triphenyl amine-substituted copper Pcs, named as OMe-DPA-CuPc and OMe-TPA-CuPc, respectively. It showed that OMe-TPA-CuPc exhibit better π-π interaction and more parallel orientations of Pcs cores in bulk aggregates compared to OMe-DPA-CuPc, and the corresponding dopant-free HTM based PSCs gave PCE of 19.7%.[37] Substitution with methoxy triphenylamine moieties highlights the strong potential to future design Pc derivatives as dopant-free HTM. Thiophenes or its derivatives as the π-linker are widely investigated as organic semiconducting materials in thin-film devices.[42,43] Particularly, thienyl groups are employed to synthesize dopant-free small molecules HTMs,[43–45] but reports dealing with Pcs analogs with thiophene or its derivatives are in scarce.[29,46,47]

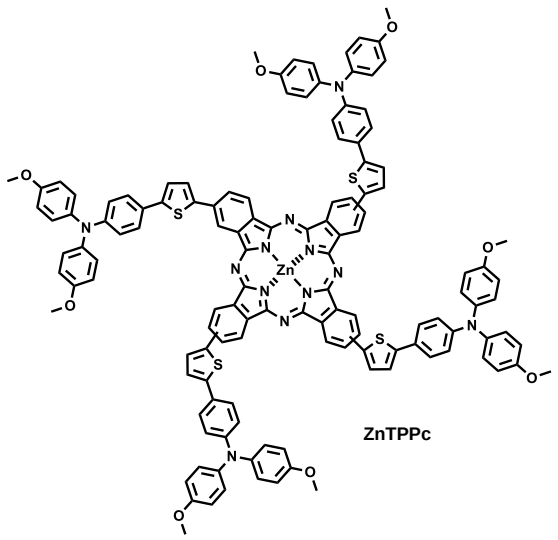

Fig.1 Chemical structure of **ZnTPPc**.

In this work, guided by rational design, we synthesize and characterize Zinc (II) 2,9,16,23-tetra-thienyl-methoxytriphenylamine-29*H*,31*H*-phthalocyanine, named as **ZnTPPc** (**Fig. 1)**, and its integration as a dopant-free HTM in PSCs is investigated. Notably, the PSC based on dopant-free **ZnTPPc** delivered a PCE of 14.5%, which is very competitive to that of the device employing the well-known undoped HTMs. Particularly, the facile synthesis of **ZnTPPc** based on commercial precursor materials makes it a promising new class of HTMs with high stability.

Results and discussion

Synthesis and characterization of ZnTPPc

Our objective was to synthesize a tetrasubstituted **ZnTPPc** with triphenylamine-thienyl conjugated aromatic electron-rich substituents. These substituents were selected in order to improve the solubility and hole mobility of Pc as a HTM. **ZnTPPc** was synthesized from autocondensation of phthalonitrile **2** in the presence of $Zn(OAc)_2$ and a drop of DBN as catalyst with 52% of yield (**Scheme 1**). The phthalonitrile **2** was obtained by Suzuki coupling of arylboronate and bromo-thienyl-phthalonitrile **3**, which in turn can be easily prepared from 4-(thiophen-2-yl)phthalonitrile **4** by bromination with NBS. Phthalonitrile **4** was synthesized by a Suzuki reaction of 4-iodophthalonitrile and thiophene-2-boronic acid pinacol ester. Palladium acetate was the best catalyst for this reaction, better than the usual $Pd_2(dba)_3$. The phthalonitriles **2-4** were characterized by ^{1}H-NMR and ^{13}C-NMR spectroscopy (Fig. S1-S6, ESI†).

The final product **ZnTPPc** was systematically characterized by ^{1}H-NMR spectroscopy, HR-MALDI-TOF mass spectrometry UV-vis absorption and fluorescence spectra. The ^{1}H-NMR spectra in DMSO-d_6 of **ZnTPPc** showed broad aromatic signals meanwhile the aliphatic ones are well defined. This may be due to aggregation by stacking and to the presence of four different region isomers (Fig. S7, ESI†). The absorption spectra of **ZnTPPc** in DMF (Fig. 2a) presented the Soret bands located in the ultraviolet region around 390 nm and the Q band in the region between 600 nm and 780 nm. Intensive absorptions at 647 nm and 719 nm, respectively, could be ascribed to strong π–π* transitions of Q-band.[37] The ZnTPPc show strong, narrow steady-state fluorescence with peak position at 768 nm (Fig. 2a). The optical bandgap (E_g) of **ZnTPPc** was estimated from the corresponding intersection of absorption and fluorescence spectra, thus, resulting in 1.65 eV.

The electrochemical characterization was performed to evaluate the energy level alignment of the perovskite/**ZnTPPc** interface via using cyclic voltammetry as displayed in Fig. 2b. The ferrocene redox couple was used as the external standard and **ZnTPPc** showed two oxidation peaks at 0.35 V and 0.79 V (vs Fc/Fc^{+}), respectively. The highest occupied molecular orbital energy level (E_{HOMO}) of **ZnTPPc** was calculated according to Equation: E_{HOMO}=-4.8-E_{ox}, where E_{ox} is the first onset oxidation potential. The E_{HOMO} value was estimated to be -5.15 eV and located in between valence band of perovskite (-5.9 eV) and work function of gold (-5.1 eV), which could facilitate the hole carrier extraction from perovskite to metal electrode.[48] While the lowest unoccupied molecular orbital energy level (E_{LUMO}) of **ZnTPPc** was -3.44 eV, determined by adding the previously obtained E_g to E_{HOMO} value. E_{LUMO} lies higher than the conduction band of perovskite (-4.4 eV), which can efficiently block the photo-generated electron and avoid recombination at the interface of perovskite/HTM.

Particularly, the charge transporting abilities of HTMs are crucial to fabricate high-performance PSCs and the conductivity and hole mobility of **ZnTPPc** were firstly studied. The electrical conductivity was determined by measuring the current-voltage (*I-V*) curve of the device in a structure (FTO/HTM/Ag) following the equation of $\sigma = IA^{-1}V^{-1}d$, where A is the active area of the device, *d* is the thickness of HTM.

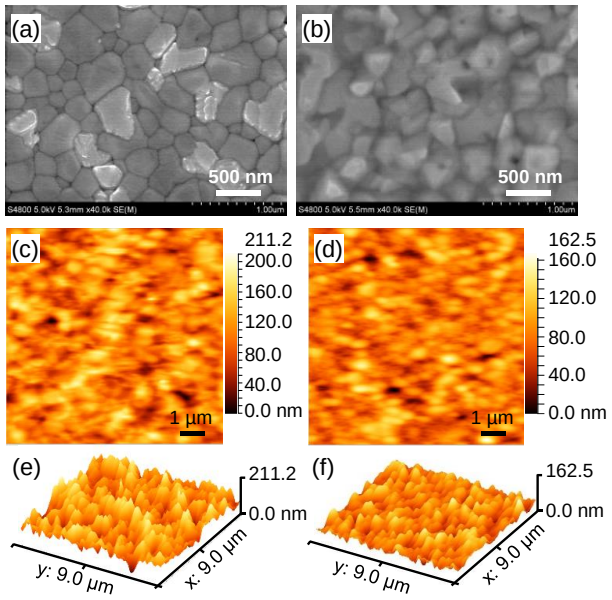

Fig.3 Top-view SEM images of (a) perovskite and (b) perovskite/ZnTPPc film. AFM height images of the (c) perovskite and (d) perovskite/ZnTPPc. Corresponding 3D AFM images of the (e) perovskite and (f) perovskite/ZnTPPc film.

The calculated conductivity of **ZnTPPc** was found to be 2.9×10^{-6} S cm^{-1}, and for pristine Spiro-OMeTAD was 6.9×10^{-7} S cm^{-1}, showing the similar values reported elsewhere (10^{-7}- 10^{-8} S cm^{-1}).[10,49] The conductivity value of ZnTPPc is notably one magnitude higher than the value of pristine Spiro-OMeTAD. Besides, the hole mobility of the **ZnTPPc** and pristine Spiro, was evaluated by space charge limited current (SCLC) method using a hole-only device with the architecture of FTO/PEDOT:PSS/**HTM**/Ag. The current density-voltage (*J-V*) curve was tested under the dark and ambient condition and the hole mobility was calculated using the Mott-Gurney law ($J=9\varepsilon\varepsilon_0\mu V_{app}^2/8d^3$). The obtained hole mobility of **ZnTPPc** was 4.1×10^{-5} cm^2 V^{-1} s^{-1}, which is higher than that of pristine Spiro-OMeTAD (1.7×10^{-5} cm^2 V^{-1} s^{-1}).[50,51] The relatively higher conductivity and mobility of ZnTPPc will allow improvement of in charge transporting ability and fill factor thus device performance.

The film-forming ability of **ZnTPPc** was investigated with the help of microscopy techniques such as scanning electron microscopy (SEM) and atomic force microscopy (AFM). The **Fig. 3a & 3b** showed the top-view SEM of bare perovskite and perovskite covered with **ZnTPPc** (perovskite/**ZnTPPc**), respectively. Compared to bare perovskite, the surface microstructure of perovskite/**ZnTPPc** film shows full-coverage without any voids or defects. **Fig. 3c & 3d**, suggests similar observation with AFM topographical images and bare perovskite film displayed a root mean square (RMS) roughness value of 29.1 nm. The surface of perovskite/**ZnTPPc** becomes smoother and decreased RMS value of 19.6 nm was noted. The uniform, smooth HTM film can extract photo-generated holes effectively and avoid interfacial recombination loss, and improve the device performance. In all, the **ZnTPPc** armed with such excellent properties such as matched energy level with perovskite and improve electrical properties, film-forming ability demonstrates great potential towards fabricating efficient PSCs.

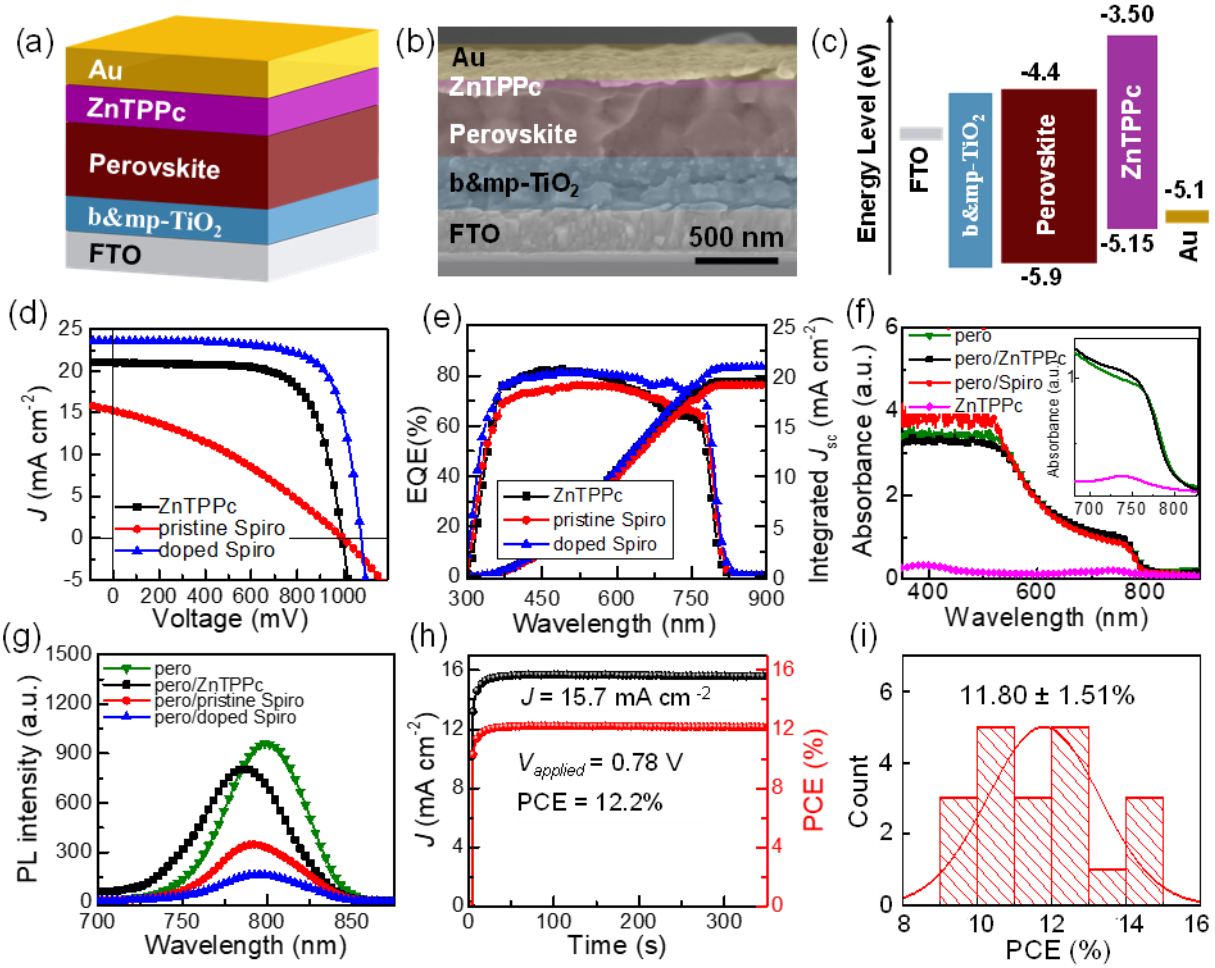

Fig. 4 (a) Device structure , (b) cross-sectional SEM images of the PSCs with ZnTPPc, (c) schematic of the energy level of the PSCs with ZnTPPc, (d) *J-V* curves characterized under simulated AM 1.5G illumination for the devices with different HTMs, (e) EQE and Integrated J_{sc} of the champion device based on different HTMs, (f) absorbance spectra of different thin films, (g) steady state photoluminescence spectra of perovskite with different HTMs, (h) steady-state power output at the maximum power point for the champion device with ZnTPPc as HTM and (i) histograms of PCE performance parameters of PSCs with ZnTPPc as an HTM. The data was analyzed from 20 cells, Spiro-OMeTAD is referred as Spiro.

Photovoltaic performance of PSCs with ZnTPPc as HTM

To validate the potential of **ZnTPPc** as an efficient HTM in PSCs, we fabricated devices with an architect of FTO/*b*&*mp*-TiO_2/perovskite/**ZnTPPc**/Au (*b*&*mp*-TiO_2 presents blocking and mesoporous TiO_2 layer, **Fig 4a**) and for comparative purpose, pristine and doped Spiro-OMeTAD were used as reference HTM. Fig 4b shows a representative cross-sectional SEM image of PSC device with **ZnTPPc** as an HTM, where the mixed perovskite atop of *mp*-TiO_2 was prepared by a two-step deposition method and the thickness was ~ 450 nm.[17,18,25] A thin layer of **ZnTPPc** covered on perovskite film allows around 60 nm thick film. The energy level diagram (Fig. 3c) of **ZnTPPc** based device shows a well matched HOMO-LUMO energy level with respect the perovskite and thus exhibit the stronger possibility of transporting the holes efficiently. The *J-V* curves of the champion device with different HTMs were measured under reverse scan and corresponding photovoltaic parameters are shown in Fig. 4d and **Table 1.** The PSC with **ZnTPPc** yielded an overall PCE of 14.5%, with an open-circuit voltage (V_{oc}) of 994.3 mV, a short circuit current density (J_{sc}) of 21.0 mA cm^{-2}, and a fill factor (*FF*) of 69.42%. A reference device with conventional Spiro-OMeTAD doped with lithium bis(trifluoromethanesulfonyl)imide (LiTFSI) and 4-tert-Butylpyridine (t-BP) was fabricated with the same condition, and exhibited a PCE of 18.47% with a V_{oc} of 1075.9 mV, a J_{sc} of 23.62 mA cm^{-2}, and a FF of 72.69%, which was slightly higher than that of the device with pristine **ZnTPPc**. However, when using pristine Spiro-OMeTAD as a HTM, the device showed inferior PV parameters and registered a PCE of 5.14%, with a V_{oc} of 993.9 mV, J_{sc} of 15.25 mA cm^{-2}, *FF* of 33.92%. Notably, low J_{sc} and FF was found due to the poor electrical properties of Spiro-OMeTAD in its pristine form. The series resistance (R_s) of different HTMs are shown in Table 1. The **ZnTPPc**-based device displayed the R_s of 58 Ω, which is comparable with the value of doped Spiro-OMeTAD device (44 Ω) and lower than the value of pristine Spiro-OMeTAD device (424 Ω). Subsequently, the relative low R_s of **ZnTPPc**-based device allowed us to achieve improved FF and subsequently PCE.[52–54]

Fig. 4e presents the external quantum efficiency (EQE) spectra and the integrated current density (integrated J_{sc}). The integrated J_{sc} values of PSCs with **ZnTPPc**, pristine and doped Spiro-OMeTAD are 19.41, 19.06, and 20.86 mA cm^{-2}, respectively, close to the J_{sc} value attained from *J-V* curves
under the standard solar AM 1.5G. The lower J_{sc} value of the **ZnTPPc**-based device obtained from EQE spectra compared with doped Spiro-OMeTAD is in agreement with the value from the *J-V* curves. The device with **ZnTPPc** and Spiro-OMeTAD own the same EQE value at wavelength ranging from 300 nm to 580 nm, while the device with **ZnTPPc** showed lower EQE value than that of the device with Spiro-OMeTAD at wavelength ranging from 580 nm to 800 nm. Considering the strong absorbance of Pcs at wavelength ranging from 580 nm to 800 nm (Fig. 1a & 4f), one possible reason of decreased EQE and J_{sc} of **ZnTPPc**-based device is that unabsorbed long-wavelength light passing through the perovskite active layer was absorbed by ZnTPPc instead of being reflected by the electrode and reabsorbed by the perovskite layer, leading to the decrease of photocurrent and efficiency.
Photoluminescence (PL) characterization for perovskite with different HTMs on the quartz substrate was used to analyse the charge carrier separation and transport process.[55–58] In order to observe the hole extraction ability of different HTMs, steady state photoluminescence (PL) measurement was made with the
structure of quartz/perovskite/HTM. Fig. 4g. shows the steady state PL spectra for pristine perovskite and with different HTM excited from the quartz side at 600 nm. The strong PL emission peak centred at 798 nm was observed for pristine perovskite while a decrease in PL intensity was noticed with all the HTM samples indicating the efficient hole extraction. Although, HTMs can quench the PL of perovskite, however, doped Spiro-OMeTAD exhibit the maximum PL quenching compared to undoped Spiro and **ZnTPPc**. Interestingly, in case of **ZnTPPc** , blue shifted PL peak (from 798 to 787 nm at the Pero/ZnTPPC was observed, which can be ascribed to a decrease in the surface trap states[59] on the surface and grain boundaries of perovskite layer, since surface roughness and film morphology was improved after **ZnTPPc** deposition as shown in Figure 3b-d. To evaluate the reliability of the device, the stabilized power output was measured (Fig. 4h). The device with **ZnTPPc** showed 15.7 mA cm^{-2} under the constant bias of near the maximum power point (0.78 V), and yielded stable PCE of 12.2%, in good agreement with the average PCE obtained from forward and reverse scan (12.92%). Besides, to check the reproducibility, 20 independent devices were statistically analysed, and the histograms of PCE (Fig. 4i) as well as V_{oc}, J_{sc} and FF (Fig. S9 ESI†) are summarized in Table 1. The average PCE was 11.80±1.51%. Our results suggest reproducibility of PSCs with **ZnTPPc** as an HTM possibly due to its core structure, which has high tolerance power and nature.

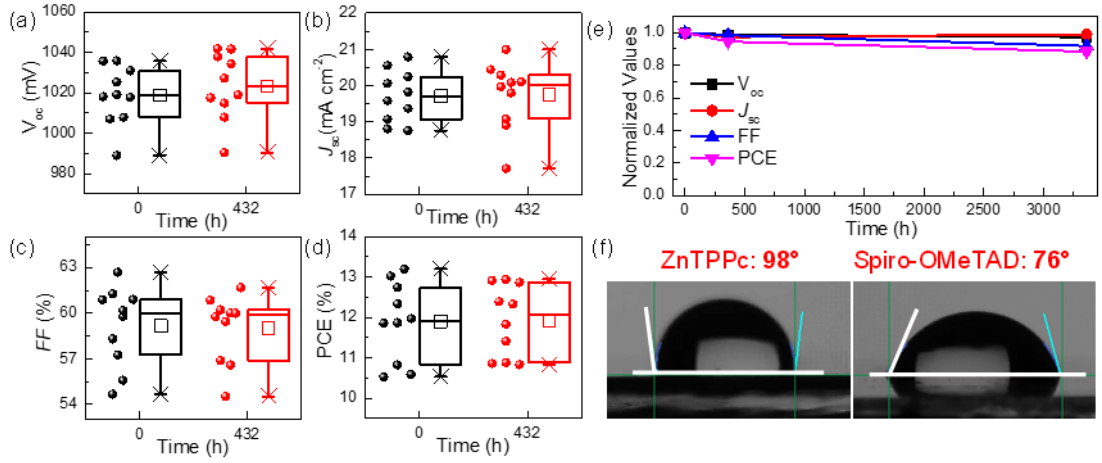

Fig. 5 Statistical box plots of the photovoltaic performance parameters of devices using **ZnTPPc** (a- d) vs storage time; the data was analysed from 20 cells, (e) normalized values of device performance parameters of ZnTPPc-based PSCs during aging and (f) contact angle value of perovskite with different HTMs.

Table 1. Photovoltaic parameters of the PSCs based on different HTMs.

HTM	V_{oc} (mV)	J_{sc} (mA cm^{-2})	FF (%)	PCE (%)	R_s (Ω)	R_{sh} (kΩ)
ZnTPPc (Pristine)	994.3	21.00	69.42	14.50	58	19.2
Pristine Spiro	993.9	15.25	33.92	5.14	424	1.7
Doped Spiro	1075.9	23.62	72.69	18.47	44	5.6
ZnTPPc (statistics)	1011.4±21	19.92±0.81	58.42±5.6	11.80±1.51		

Apart from the performance in terms of efficiency, the long-term stability of corresponding devices is another important parameter to further assess the potential of HTMs. These un-encapsulated devices were stored in a dry box under 40 - 50% relative humidity and room temperature condition. The **ZnTPPc**-based PSCs present average PCE of 12.75% after aging for 432 h, while the initial average values of the device were 12.31%, showing slight increases after aging (**Fig. 5** and **Table S2**). Such phenomena typically originated from the optimization of interface contact by solvent drying with storage time. In contrast, the average PCE of the device with doped Spiro-OMeTAD dropped from 18.28% to 16.91% after aging 120 h under similar conditions (Fig. S10 and Table S2, ESI†). Importantly, the average PCE of the **ZnTPPc**-based device remains 88% of initial efficiency after aging for over 3000 h (Fig. 5e and Table S3, ESI†). This point towards **ZnTPPc** based PSCs superior stability. The plausible reasons for improved stability are as follows: the perovskite/ZnTPPc show a higher water contact angle of 98° compared to that of Spiro-OMeTAD (76°) (Fig. 5f), the excellent hydrophobic nature of **ZnTPPc** can effectively block the water penetration into perovskite layers.

To conclude, through molecular engineering, we have designed a tetrasubstituted **ZnTPPc** with electron-rich thienyl-triphenylamine conjugated aromatic substituents. We found that **ZnTPPc** possesses superior electrical properties such as relative high conductivity and mobility compared to pristine Spiro-OMeTAD, suitable energetic level alignment and can supress the trap state on the surface of perovskite. The perovskite solar cells fabricated thereof employing **ZnTPPc** as a hole selective layer gave a highly competitive power conversion efficiency over 14.5%, without the use of any dopant and additives. Furthermore the ultrathin layer will cut down materials consumption and will further lower the cost. **ZnTPPc** maintained the initial efficiency after the aging measurement.

Experimental

Materials

Chemicals were purchased from Sigma Aldrich unless otherwise specified, whereas Na_2CO_3 was acquired from Scharlab, *N*-bromosuccinimide and K_2CO_3 from Alfa Aesar, 4-methoxy-*N*-(4-methoxyphenyl)-*N*-(4-(4,4,5,5-tetramethyl-1,3,2-dioxaborolan-2-yl)phenyl)aniline from Fluorochem, and TBAB from Fluka. All chemicals were employed without any further treatment or purification. 4-iodophthalonitrile was synthesized according to the processes described in the literature.[60]

All reactions were carried out under a nitrogen atmosphere. The solvents for spectroscopic studies were of spectroscopic grade and used as received. Column chromatography was carried out silica gel 60 ACC (40-63 µm). Thin layer chromatography was performed on TLC plates coated with SiO_2 (40-63 µm) 60F254.

Synthesis of ZnTPPc

60 mg (0.12 mmol) of **2**, 10.7 mg (0.058 mmol) of $Zn(OAc)_2$ and a drop of DBN were dissolved in 200 µL of DMAE and heated to reflux under nitrogen atmosphere for 16 h. After cooling at room temperature, DMAE was removed by distillation with toluene. The residue was passed by column chromatography (DCM:MeOH/95:5), the green solid obtained washed with MeOH at reflux, and finally purified by preparative TLC (DCM:MeOH, 96:4) affording **ZnTPPc** (32 mg, 52 %) as a green powder. UV-vis: λ_{max} (DMF)/nm (log Ɛ): 390 (5.01), 647 (4.57), 719 (5.17). HRMS (MALDI-TOF-MS): For $C_{128}H_{92}N_{12}O_8S_4Zn$ $(M)^+$ calc. 2116.533, found 2116.581.

Synthesis of phthalonitrile 2

200 mg (0.69 mmol) of **3**, 300 mg (0.69 mmol) of 4-methoxy-*N*-(4-methoxyphenyl)-*N*-(4-(4,4,5,5-tetramethyl-1,3,2-dioxaborolan-2-yl)phenyl)aniline, 63.4 mg (0.069 mmol) of $Pd_2(dba)_3$, 145.2 mg (0.55 mmol) of PPh_3 and 11.4 mg (0.035 mmol) of TBAB were dissolved in 16 mL of degassed toluene. A degassed 2M solution of K_2CO_3 was added and heated to 90 °C under nitrogen atmosphere for 24 hours. After cooling at room temperature, the crude was filtered and concentrated. Purification by column chromatography using hexane:ethyl acetate (7:3) afforded **2** (168 mg, 48%) as a red powder. ^{1}H NMR ($CDCl_3$): δ = 3.81 (s, 6H), 6.89 (m, 6H), 7.09 (m, 4H), 7.22 (d, *J*= 3.9, 1H), 7.42 (m, 3H), 7.75 (dd, *J*= 8.3, 0.4, 1H), 7.86 (dd, *J*= 8.3, 1.9, 1H), 7.96 (dd, *J*= 1.9, 0.4, 1H). ^{13}C NMR ($CDCl_3$): δ = 55.5, 112.3, 114.8, 115.3, 115.6, 116.6, 119.7, 123.1, 124.6, 126.5, 127.0, 127.6, 128.5, 129.3, 133.9, 136.5, 139.5, 140.1, 148.6,

149.3, 156.4. UV-vis: λ_{max} ($CHCl_3$)/nm (log ε): 451 (4.39). HRMS (MALDI-TOF-MS): For $C_{32}H_{23}N_3O_2S$ $(M)^+$ calc. 513.151 found 513.122.

Synthesis of phthalonitrile 3

500 mg (2.38 mmol) of **4** were dissolved in 12 mL of DCM and cooled to 0 °C. A solution of 634.8 mg (3.57 mmol) of *N*-bromosuccinimide (NBS) dissolved in 12 ml of acetic acid was added dropwise for 30 minutes, and stayed at room temperature overnight. The reaction was carried in darkness. Then it was cooled to 0 °C, the solid obtained was filtered and washed with hexane (410 mg, 60 %). ^{1}H NMR ($CDCl_3$): δ = 7.15 (d, *J*= 4.0, 1H), 7.25 (d, *J*= 4.0, 1H), 7.80 (s, 1H), 7.80 (s, 1H), 7.90 (t, *J*= 1.2, 1H). ^{13}C NMR ($CDCl_3$): δ = 112.5, 114.3, 114.6, 114.8, 115.7, 126.6, 128.5, 128.9, 131.1, 133.5, 137.6, 140.0.

Synthesis of phthalonitrile 4

1 g (3.94 mmol) of 4-iodophthalonitrile, 910 mg (4.33 mmol) of thiophene-2-boronic acid pinacol ester, 42 mg (0.19 mmol) of palladium(II) acetate and 206.5 mg (0.79 mmol) of triphenylphosphine were dissolved in 10 mL of distilled and degassed 1,4-dioxane. Then, 4 mL of a degassed 2M solution of Na_2CO_3 was added and heated to 95°C under nitrogen atmosphere for 6h. After cooling at room temperature, the crude was treated with NH_4Cl 2M, extracted with DCM, washed with distilled water, dried over $NaSO_4$, filtered and concentrated to afford a white solid. Purification by column chromatography using hexane:toluene (1:4) as solvent, afforded **4** (680 mg, 83 %) as a white powder. ^{1}H NMR ($CDCl_3$): δ = 7.18 (dd, *J*= 5.0, 3.8, 1H), 7.50 (m, 2H), 7.80 (d, *J*= 8.3, 1H), 7.91 (dd, *J*= 8.3, 1.9, 1H), 8.00 (d, *J*= 1.9, 1H). ^{13}C NMR ($CDCl_3$): δ = 111.9, 114.4, 114.6, 115.4, 126.0, 127.9, 128.1, 128.7, 129.0, 133.3, 138.5, 138.6.

Measurements for materials

NMR spectra were measured with a Bruker AC 300. UV-vis were recorded with a Helios Gamma spectrophotometer. Fluorescence spectra were recorded with a Perkin Elmer LS 55 Luminescence spectrophotometer. High-resolution mass spectra were obtained from a Bruker Microflex LRF20 matrix assisted laser desorption/ionization time of flight (MALDI-TOF) using dithranol as matrix.

Cyclic voltammetry was measured in a conventional three-electrode cell using a μ-AUTOLAB type III potentiostat/galvanostat at 298 K over benzonitrile and deaerated sample solutions containing 0.10 M tetrabutylammonium hexafluorophosphate ($TBAPF_6$) as supporting electrolyte. Platinum as working electrode, $Ag/AgNO_3$ as the reference electrode, and platinum as wire counter electrode were employed. Ferrocene/Ferrocenium was used as an internal standard for all measurements.

Device fabrication and characterization

The pre-cleaned FTO (NSG10) substrates were treated with UV-ozone machine for 60 min each time and were heated to 500 °C. A compact blocking layer of TiO_2 were deposited by spray pyrolysis using a 5% titanium (IV) diisopropoxide bis(acetylacetonate) solution diluted by anhydrous ethanol. The substrates were kept at 500 °C for 30 min after the spraying. Mesoporous TiO_2 films were obtained by spin-coating a mesoporous dispersion of TiO_2 nanoparticles (30 NRD from Dyesol) and heated at 500 °C for 30 min to produce the mesoporous structure. The substrates were transferred to an argon-filled glovebox for depositing perovskite films. The two-step deposition method was adopted to prepare perovskite . In short, 1.3M PbI_2 precursor solution dissolving in a mixed solvent (volume ratio of DMF/DMSO=9.5/0.5) was spin coating at 2,000 rpm for 20 s to prepare PbI_2 layer. The mixed organic precursor solution containing formamidinium iodide: methylammonium bromide: methylammonium chloride= 60: 6: 6 in 1 mL isopropanol was dynamically added to the PbI_2 layer and was spin-coated at 2,000 rpm for 20 s. The as-prepared film was annealed at 150 °C for 15 min in the glovebox. The **ZnTPPc** film layer was deposited atop perovskite films at a spin rate of 4,000 rpm for 20 s with 10 mM (~ 21 mg/mL) solution with chlorobenzene as the solvent. The Spio-OMeTAD hole transporting layer was prepared by spin-coated the Spiro-OMeTAD solution prepared by dissolving 72.3 mg material in 1 mL chlorobenzene. Finally, a ~ 70 nm gold electrode was deposited on top of the hole-transporting layer by thermal evaporation. *J–V* curves were recorded with a Keithley 2400 source-measurement-unit under AM 1.5 G, 100 mW cm^2 illumination from a 450 W 3A solar simulator (ORIEL, 94023 A). This was calibrated using an NREL certified calibrated monocrystalline silicon solar cell. Testing parameters: active area defined by black masks: 0.09 cm^2, scan rate: 100 mV s^{-1}, pre-sweep delay: 10 s). Surface and cross-sectional SEM images were recorded by using a Hitachi S-4800. The EQE spectra was measured using a 150 W Xenon lamp (Newport) attached to IQE200B (Oriel) motorized 1/4m monochromator as the light source. The water contact angle was tested by contact angle goniometer (Ossila). Absorption spectra was collected by Cary 60. Atomic Force Microscopy (AFM) images were acquired with CSI Nano observer AFM.

Acknowledgements

This work received funding from the European Union H2020 Programme under a European Research Council Consolidator grant [MOLEMAT, 726360]. We gratefully acknowledge the financial support provided by European Regional Development Fund ‘‘A way to make Europe and the Spanish Ministerio de Ciencia e Innovacion, Agencia Estatal de Investigación: project CTQ2017-87102-R AEI/FEDER, UE. P.H. acknowledges funding from the European Commission via a Marie-Skłodowska-Curie individual fellowship (Grant Number 896211_SMILIES). We thanks David Payno for LabVIEW software.

References

1 *https://www.nrel.gov/pv/cell-efficiency.html*, (accessed: July 2019).
2 A. Kojima, K. Teshima, Y. Shirai and T. Miyasaka, *J. Am. Chem. Soc.*, 2009, **131**, 6050–6051.
3 J. Burschka, N. Pellet, S. J. Moon, R. Humphry-Baker, P. Gao, M. K. Nazeeruddin and M. Grätzel, *Nature*, 2013, **499**, 316–319.
4 M. Liu, M. B. Johnston and H. J. Snaith, *Nature*, 2013, **501**, 395–398.
5 H.-S. Kim, C.-R. Lee, J.-H. Im, K.-B. Lee, T. Moehl, A. Marchioro, S.-J. Moon, R. Humphry-Baker, J.-H. Yum, J. E. Moser, M. Grätzel and N.-G. Park, *Sci. Rep.*, 2012, **2**, 591.
6 S. D. Stranks, G. E. Eperon, G. Grancini, C. Menelaou, M. J. P. Alcocer, T. Leijtens, L. M. Herz, A. Petrozza and H. J. Snaith, *Science* , 2013, **342**, 341–344.
7 C. S. Ponseca Jr., T. J. Savenije, M. a. Abdellah, K. B. Zheng, A. P. Yartsev, T. T. Pascher, T. Harlang, P. Chabera, T. Pullerits, A. Stepanov, J.-P. P. Wolf and V. Sundstrom, *J. Am. Chem. Soc.*, 2014, **136**, 5189–5192.
8 M. Salado, M. Andresini, P. Huang, M. T. Khan, F. Ciriaco, S. Kazim and S. Ahmad, *Adv. Funct. Mater.*, 2020, **30**, 1910561.
9 E. H. Jung, N. J. Jeon, E. Y. Park, C. S. Moon, T. J. Shin, T.-Y. Yang, J. H. Noh and J. Seo, *Nature*, 2019, **567**, 511–515.
10 L. Caliò, M. Salado, S. Kazim and S. Ahmad, *Joule*, 2018, **2**, 1800–1815.
11 S. Kazim, F. J. Ramos, P. Gao, M. K. Nazeeruddin, M. Grätzel and S. Ahmad, *Energy Environ. Sci.*, 2015, **8**, 1816–1823.
12 L. Calió, S. Kazim, M. Grätzel and S. Ahmad, *Angew. Chemie - Int. Ed.*, 2016, **55**, 14522–14545.
13 D. Li, J. Y. Shao, Y. Li, Y. Li, L. Y. Deng, Y. W. Zhong and Q. Meng, *Chem. Commun.*, 2018, **54**, 1651–1654.
14 K. Rakstys, C. Igci and M. K. Nazeeruddin, *Chem. Sci.*, 2019, **10**, 6748–6769.
15 J. Urieta-Mora, I. García-Benito, A. Molina-Ontoria and N. Martín, *Chem. Soc. Rev.*, 2018, **47**, 8541–8571.
16 Z. Hawash, L. K. Ono and Y. Qi, *Adv. Mater. Interfaces*, 2018, **5**, 1700623.
17 P. Huang, L. Yuan, K. Zhang, Q. Chen, Y. Zhou, B. Song and Y. Li, *ACS Appl. Mater. Interfaces*, 2018, **10**, 14796–14802.
18 P. Huang, Q. Chen, K. Zhang, L. Yuan, Y. Zhou, B. Song and Y. Li, *J. Mater. Chem. A*, 2019, **7**, 6213–6219.
19 F. Zhang, C. Xiao, X. Chen, B. W. Larson, S. P. Harvey, J. J. Berry and K. Zhu, *Joule*, 2019, **3**, 1452–1463.
20 F. Zhang, D. Bi, N. Pellet, C. Xiao, Z. Li, J. J. Berry, S. M. Zakeeruddin, K. Zhu and M. Grätzel, *Energy Environ. Sci.*, 2018, **11**, 3480–3490.
21 F. Zhang, W. Shi, J. Luo, N. Pellet, C. Yi, X. Li, X. Zhao, T. J. S. Dennis, X. Li, S. Wang, Y. Xiao, S. M. Zakeeruddin, D. Bi and M. Grätzel, *Adv. Mater.*, 2017, **29**, 1606806.
22 A. K. Jena, Y. Numata, M. Ikegami and T. Miyasaka, *J. Mater. Chem. A*, 2018, **6**, 2219–2230.
23 D. Bryant, N. Aristidou, S. Pont, I. Sanchez-Molina, T. Chotchunangatchaval, S. Wheeler, J. R. Durrant and S. A. Haque, *Energy Environ. Sci.*, 2016, **9**, 1655–1660.
24 N. Arora, M. I. Dar, A. Hinderhofer, N. Pellet, F. Schreiber, S. M. Zakeeruddin and M. Grätzel, *Science* , 2017, **358**, 768–771.
25 P. Huang, Manju, S. Kazim, G. Sivakumar, M. Salado, R. Misra and S. Ahmad, *ACS Appl. Mater. Interfaces*, 2020, **12**, 22881–22890.
26 L. Xu, P. Huang, J. Zhang, X. Jia, Z. Ma, Y. Sun, Y. Zhou, N. Yuan and J. Ding, *J. Phys. Chem. C*, 2017, **121**, 21821–21826.
27 X. Jiang, D. Wang, Z. Yu, W. Ma, H.-B. Li, X. Yang, F. Liu, A. Hagfeldt and L. Sun, *Adv. Energy Mater.*, 2019, **9**, 1803287.
28 M. Cheng, Y. Li, M. Safdari, C. Chen, P. Liu, L. Kloo and L. Sun, *Adv. Energy Mater.*, 2017, **7**, 1602556.
29 M. Urbani, G. de la Torre, M. K. Nazeeruddin and T. Torres, *Chem. Soc. Rev.*, 2019, **48**, 2738–2766.
30 L. Caliò, J. Follana-Berná, S. Kazim, M. Madsen, H.-G. Rubahn, Á. Sastre-Santos and S. Ahmad, *Sustain. Energy Fuels*, 2017, **1**, 2071–2077.
31 M. G. Walter, A. B. Rudine and C. C. Wamser, *J. Porphyr. Phthalocyanines*, 2010, **14**, 759–792.
32 M. E. Ragoussi, J. J. Cid, J. H. Yum, G. De La Torre, D. Di Censo, M. Grätzel, M. K. Nazeeruddin and T. Torres, *Angew. Chemie - Int. Ed.*, 2012, **51**, 4375–4378.
33 W. Ke, D. Zhao, C. R. Grice, A. J. Cimaroli, G. Fang and Y. Yan, *J. Mater. Chem. A*, 2015, **3**, 23888–23894.
34 J. Cao, X. Lv, P. Zhang, T. T. Chuong, B. Wu, X. Feng, C. Shan, J. Liu and Y. Tang, *Adv. Mater.*, 2018, **30**, 1800568.
35 T. Duong, J. Peng, D. Walter, J. Xiang, H. Shen, D. Chugh, M. Lockrey, D. Zhong, J. Li, K. Weber, T. P. White and K. R. Catchpole, *ACS Energy Lett.*, 2018, **3**, 2441–2448.
36 Q. Hu, E. Rezaee, M. Li, Q. Chen, Y. Cao, M. Mayukh, D. V. McGrath and Z. X. Xu, *ACS Appl. Mater. Interfaces*, 2019, **11**, 36535–36543.
37 Y. Feng, Q. Hu, E. Rezaee, M. Li, Z. Xu, A. Lorenzoni, F. Mercuri and M. Muccini, *Adv. Energy Mater.*, 2019, 1901019.
38 Y. Wang, X. Liu, H. Shan, Q. Chen, T. Liu, X. Sun, D. Ma, Z. Zhang, J. Xu and Z. X. Xu, *Dye. Pigment.*, 2017, **139**, 619–626.

39 X. Jiang, Z. Yu, H.-B. Li, Y. Zhao, J. Qu, J. Lai, W. Ma, D. Wang, X. Yang and L. Sun, *J. Mater. Chem. A*, 2017, **5**, 17862–17866.
40 D. Molina, M. A. Ruiz-Preciado, B. Carlsen, F. T. Eickemeyer, B. Yang, N. Flores-Díaz, M. J. Álvaro-Martins, K. Nonomura, A. Hagfeldt and Á. Sastre-Santos, *ChemPhotoChem*, 2020, **4**, 307–314.
41 Z. Cui, Y. Wang, Y. Chen, X. Chen, X. Deng and W. Chen, *Org. Electron.*, 2019, **69**, 248–254.
42 F. Zhang, D. Wu, Y. Xu and X. Feng, *J. Mater. Chem.*, 2011, **21**, 17590.
43 H. Li, K. Fu, P. P. Boix, L. H. Wong, A. Hagfeldt, M. Grätzel, S. G. Mhaisalkar and A. C. Grimsdale, *ChemSusChem*, 2014, n/a-n/a.
44 G. Kim, H. Choi, M. Kim, J. Lee, S. Y. Son and T. Park, *Adv. Energy Mater.*, 2020, **10**, 1903403.
45 I. Zimmermann, J. Urieta-Mora, P. Gratia, J. Aragó, G. Grancini, A. Molina-Ontoria, E. Ortí, N. Martín and M. K. Nazeeruddin, *Adv. Energy Mater.*, 2017, **7**, 1601674.
46 P. Gao, K. T. Cho, A. Abate, G. Grancini, P. Y. Reddy, M. Srivasu, M. Adachi, A. Suzuki, K. Tsuchimoto, M. Grätzel and M. K. Nazeeruddin, *Phys. Chem. Chem. Phys.*, 2016, **18**, 27083–27089.
47 K. T. Cho, O. Trukhina, C. Roldán-Carmona, M. Ince, P. Gratia, G. Grancini, P. Gao, T. Marszalek, W. Pisula, P. Y. Reddy, T. Torres and M. K. Nazeeruddin, *Adv. Energy Mater.*, 2017, **7**, 1601733.
48 Q. Jiang, L. Zhang, H. Wang, X. Yang, J. Meng, H. Liu, Z. Yin, J. Wu, X. Zhang and J. You, *Nat. Energy*, 2017, **2**, 16177.
49 W. H. Nguyen, C. D. Bailie, E. L. Unger and M. D. Mcgehee, .
50 P. Qin, S. Tanaka, S. Ito, N. Tetreault, K. Manabe, H. Nishino, M. K. Nazeeruddin and M. Grätzel, *Nat. Commun.*, 2014, **5**, 1–6.
51 D. Bi, B. Xu, P. Gao, L. Sun, M. Grätzel and A. Hagfeldt, *Nano Energy*, 2016, **23**, 138–144.
52 C. Shen, Y. Wu, H. Zhang, E. Li, W. Zhang, X. Xu, W. Wu, H. Tian and W.-H. Zhu, *Angew. Chemie Int. Ed.*, 2019, **58**, 3784–3789.
53 N. J. Jeon, H. G. Lee, Y. C. Kim, J. Seo, J. H. Noh, J. Lee and S. Il Seok, *J. Am. Chem. Soc.*, 2014, **136**, 7837–7840.
54 P. Huang, Z. Wang, Y. Liu, K. Zhang, L. Yuan, Y. Zhou, B. Song and Y. Li, *ACS Appl. Mater. Interfaces*, 2017, **9**, 25323–25331.
55 P. Liu, B. Xu, Y. Hua, M. Cheng, K. Aitola, K. Sveinbjörnsson, J. Zhang, G. Boschloo, L. Sun and L. Kloo, *J. Power Sources*, 2017, **344**, 11–14.
56 X. Liu, F. Zhang, Z. Liu, Y. Xiao, S. Wang and X. Li, *J. Mater. Chem. C*, 2017, **5**, 11429–11435.
57 F. Zhang, Z. Wang, H. Zhu, N. Pellet, J. Luo, C. Yi, X. Liu, H. Liu, S. Wang, X. Li, Y. Xiao, S. M. Zakeeruddin, D. Bi and M. Grätzel, *Nano Energy*, 2017, **41**, 469–475.
58 F. Zhang, S. Wang, H. Zhu, X. Liu, H. Liu, X. Li, Y. Xiao, S. M. Zakeeruddin and M. Grätzel, *ACS Energy Lett.*, 2018, **3**, 1145–1152.
59 D. W. DeQuilettes, S. M. Vorpahl, S. D. Stranks, H. Nagaoka, G. E. Eperon, M. E. Ziffer, H. J. Snaith and D. S. Ginger, *Science* , 2015, **348**, 683–686.
60 S. M. Marcuccio, P. I. Svirskaya, S. Greenberg, A. B. P. Lever, C. C. Leznoff and K. B. Tomer, *Can. J. Chem.*, 1985, **63**, 3057–3069.